Journal of Physics and Chemistry of Solids 208 (2026) 113077

Contents lists available at ScienceDirect

Journal of Physics and Chemistry of Solids

journal homepage: www.elsevier.com/locate/jpcs

Electrical and dielectric properties of colossal permittivity co-doped (Er,Pr, Ta) titanium dioxide

Lucas A.S. Ferreira, Reginaldo Muccillo, Eliana N.S. Muccillo *

Energy and Nuclear Research Institute (IPEN), Center of Science and Technology of Materials, 05508-000, São Paulo, SP, Brazil

ARTICLE INFO

Keywords:
Titanium dioxide
Co-dopants
Impedance spectroscopy
Electric permittivity

ABSTRACT

The electrical and dielectric properties of titanium dioxide containing erbium and praseodymium oxides as acceptors, and tantalum oxide as donor dopants were investigated aiming to identify the effects of different dopants on the dielectric properties. Dense samples with 1 mol% total co-dopants were prepared by the solid-state synthesis method, followed by conventional sintering at 1450 °C. A secondary phase, $Er_2Ti_2O_7$, was found in some of the prepared samples. Impedance spectroscopy spectra of the samples are similar, with an average activation energy for interface conduction of about 0.27 ± 0.05 eV, except for the sample with excess Ti, $(Er_{0.5}Ta_{0.5})_{0.01}Ti_{1.09}O_2$, (0.38 ± 0.05 eV). All samples exhibit colossal permittivity (>10^4) in wide temperature and frequency ranges. Erbium oxide was found to be more effective in increasing the electric permittivity of TiO_2 than praseodymium oxide. Excess titanium leads to a larger grain size, and decreases both the permittivity and the dissipation factor of titanium dioxide.

1. Introduction

Among the several classes of electroceramics, those with very high electric permittivity (ε′) find application in a variety of technologies, with emphasis in microelectronics and high-energy density storage devices [1–3].

The best-known dielectric ceramics with colossal permittivity (ε' ≥ 10^3) are $BaTiO_3$, $SrTiO_3$, co-doped NiO, $CaCu_3Ti_4O_{12}$ and co-doped TiO_2 [1,4–8]. Other relevant properties for technological applications are stability over wide temperature and frequency ranges and a low dissipation factor (tan δ). These requirements are not easily achieved, and the search for new compositions or optimizations in the processing of materials to maximize their performance is still a subject of work [9–12].

Several mechanisms have been proposed to explain the outstanding values of the electric permittivity found in some dielectric ceramics. Nonetheless, special attention has been given to Internal Barrier Layer Capacitance (IBLC) and Surface Barrier Layer Capacitance (SBLC) models. These models are based on the extrinsic Maxwell-Wagner type effect, which derives from the buildup of charges at interfaces, typically the grain boundaries and interfaces, or at the external surfaces [13–15].

In 2013 a new mechanism named Electron Pinned Defect Dipoles (EPDD) based on defect reactions was proposed to be effective in co-doped TiO_2 [8]. Since then, intensive research work has been carried out in co-doped titanium dioxide ceramics [8–12,16–24]. According to the EPDD model, the introduction of a donor cation (such as Ta^{5+}) in the crystal lattice of TiO_2 induces reduction of Ti^{4+} to Ti^{3+} and an electron is created for charge compensation. In addition, the inclusion of an acceptor cation (for example M^{3+}) increases the concentration of oxygen vacancies. These defect reactions are represented in Eqs. (1)–(3):

$$2TiO_2 + Ta_2O_5 \xrightarrow{4TiO_2} 2Ti'_{Ti} + 2Ta_{Ti} + 8O_O + \frac{1}{2}O_2 \quad (1)$$

$$Ti^{4+} + e' \rightarrow Ti^{3+} \quad (2)$$

$$M_2O_3 \xrightarrow{2TiO_2} 2M'_{Ti} + V_{\ddot{O}} + 3O_O \quad (3)$$

These point defects form triangular and diamond-shaped defects, which are strongly correlated leading to clusters, where the electrons are trapped. The main difference between the models based on the Maxwell-Wagner effect and the EPDD defect reactions, is that the formers act on interfaces (internal or external), whereas the latter is more effective in the bulk of the dielectric ceramics. A recent review on the main dielectric ceramics with colossal permittivity indicates that

* Corresponding author. Energy and Nuclear Research Institute - IPEN, Center of Science and Technology of Materials, University City, S. Paulo, 05508-000, SP, Brazil.
E-mail address: enavarro@usp.br (E.N.S. Muccillo).

https://doi.org/10.1016/j.jpcs.2025.113077
Received 26 May 2025; Received in revised form 17 July 2025; Accepted 3 August 2025
Available online 5 August 2025

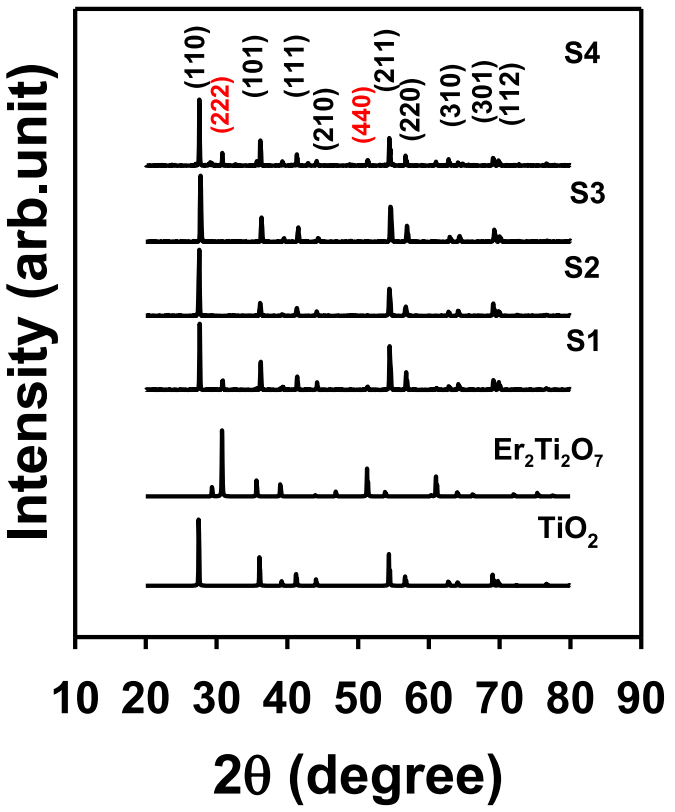

Fig. 1. XRD patterns of rutile TiO_2 (PDF 21–1276), pyrochlore $Er_2Ti_2O_7$ (PDF 18–499), and sintered samples. The main peaks of the pyrochlore phase are highlighted in red.

discrepancies concerning the underlying mechanism persist [3].

One approach to optimize the properties of ceramic materials, especially those with semiconductor behavior, is by controlling the interface properties. The interfaces, as a rule, interact with the bulk leading to strain effects, chemical interdiffusion, space charge formation and others [25].

The influence of interfaces on electrical and dielectric properties of ceramic materials is usually studied by electrochemical impedance spectroscopy. Under specific circumstances, this non-destructive technique allows for measuring the frequency-dependent electrical responses of the bulk, interfaces and electrodes, providing insights in interface phenomena, charge transport and dielectric behavior [26].

In this work, the effects of erbium oxide and praseodymium oxide as acceptor cations, and tantalum oxide as donor cation on the electrical and dielectric properties of titanium dioxide were evaluated by electrochemical impedance spectroscopy. The influence of a dissimilar content of the acceptor and donor cations and of excess of Ti were also investigated for the first time in samples containing erbium oxide to reveal their effects on the electric permittivity and dissipation factor of the co-doped ceramics.

2. Experimental

2.1. Sample preparation

Titanium oxide (rutile, 99.5 %, Alfa Aesar), tantalum oxide (99 %, Alfa Aesar), erbium oxide (99.9 %, Sigma Aldrich) and praseodymium (III, IV) oxide (99.999 %, Strem Chemicals) were the starting materials. The nominal compositions with fixed total co-dopants content (1 mol%) were: $(Er_{0.5}Ta_{0.5})_{0.01}Ti_{0.99}O_2$, $(Pr_{0.5}Ta_{0.5})_{0.01}Ti_{0.99}O_2$, $(Er_{0.25}Ta_{0.75})_{0.01}Ti_{0.99}O_2$ and $(Er_{0.5}Ta_{0.5})_{0.01}Ti_{1.09}O_2$, hereafter referred as S1, S2, S3 and S4, respectively.

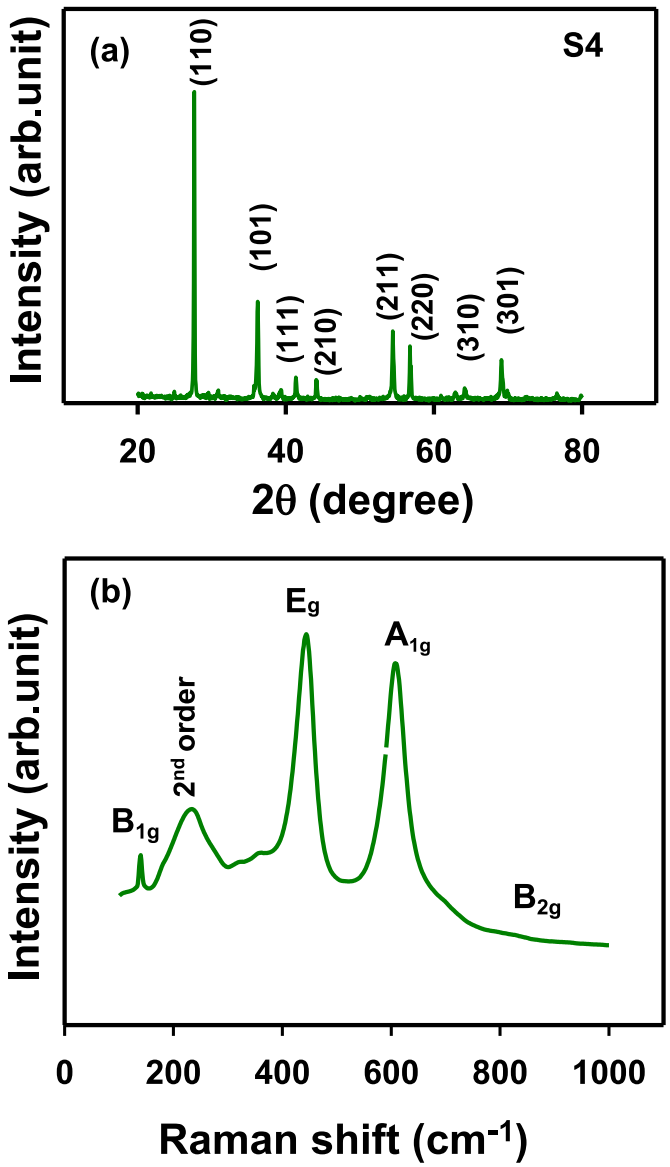

Fig. 2. (a) XRD pattern and (b) Raman spectrum of sample S4 after sanding the surface.

Table 1
Crystalline phase, relative density (ρ_r) and porosity (p_a) of sintered samples.

Sample	Crystalline phase[a]	ρ_r (%)	p_a (%)
S1	t + p	96.2 ± 0.1	1.0 ± 0.6
S2	t	96.8 ± 0.2	1.3 ± 0.6
S3	t	97.0 ± 0.2	0.5 ± 0.1
S4	t + p	94.6 ± 0.1	1.8 ± 0.1

[a] t = tetragonal; p = pyrochlore $Er_2Ti_2O_7$.

These compositions were prepared in triplicate by the solid-state synthesis method. The starting oxides were dried at 100 °C for 12 h, weighed in the stoichiometric proportions and ball-milled for 5 h with zirconia balls (ϕ 2 mm, YTZ, Tosoh) in isopropyl alcohol medium. After drying the milled powders, an organic binder (polyvinyl alcohol, PVA, 3 wt%) was added and dispersed with ultrasound. Cylindrical ceramics were obtained by uniaxial pressing (ϕ 8 mm, 2–3 mm thickness) at 20 MPa (Z2T, Kratos), followed by cold isostatic pressing at 200 MPa (National Forge Co.). The green ceramics were sintered at 1450 °C for 2 h in air with 5 °C.min^{-1} heating and cooling rates.

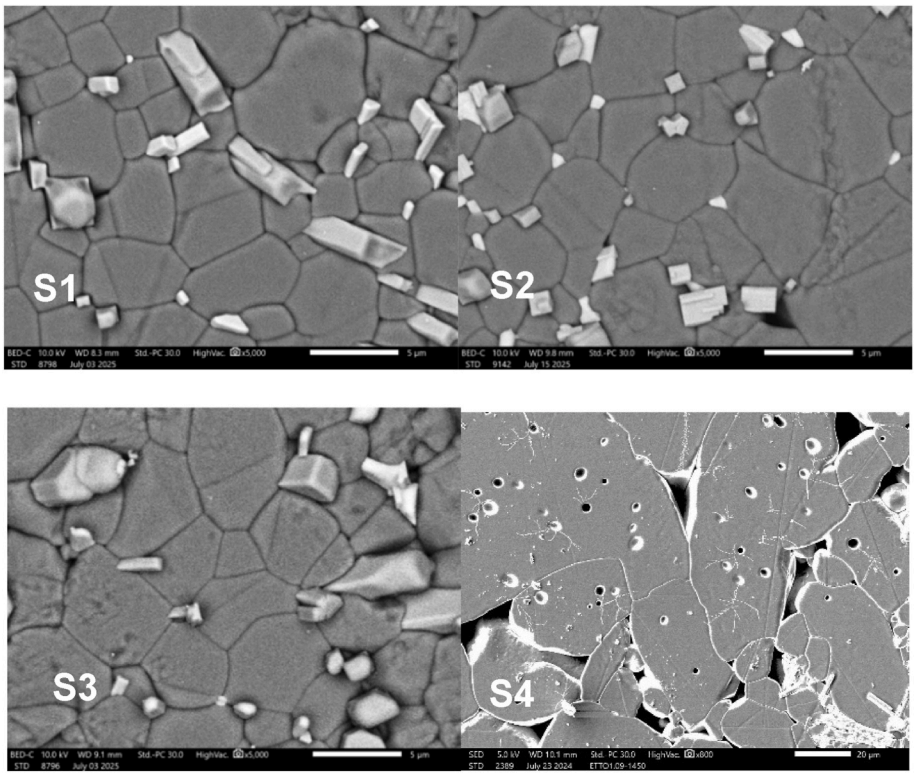

Fig. 3. SEM micrographs of sintered samples. Bar length = 5 μm (S1, S2 and S3) and 20 μm (S4).

2.2. Characterization

The apparent density and porosity of sintered ceramics were evaluated by the Archimedes method with distilled water. The phase composition and crystal structure of sintered ceramics were examined by X-ray diffraction, XRD, in a diffractometer (Bruker-AXS, D8 Advance), with Cu K_α radiation ($\lambda = 1.5405$ Å) in the 20°–80° 2θ range, and 0.05° step size and 3 s per step, and by Raman spectroscopy (Horiba, XploRA™ PLUS) with 785 nm laser in the 100 to 1000 cm^{-1} range. Microstructure features were observed by field emission gun scanning electron microscopy, SEM (Jeol, JSM-IT700 HR) and energy dispersive spectroscopy, EDS.

Electrical and dielectric characterizations of sintered ceramics were carried out by electrochemical impedance spectroscopy (HP 4192A) in the 5 Hz to 13 MHz frequency range, with 200 mV of applied AC signal. The measurements were performed in the ~40–~215 °C range with 50 min of dwell time at each temperature. Silver paste was applied onto the large surfaces of pellets to act as electrode, and curing was carried out at 400 °C. The impedance spectroscopy spectra were fitted with EIS Spectrum Analyzer.

3. Results and discussion

Fig. 1 shows the XRD patterns of sintered ceramics along with those of rutile TiO_2, PDF 21–1276, and $Er_2Ti_2O_7$ pyrochlore-type phase, PDF 18–499.

All samples display the tetragonal structure of TiO_2 as a major crystalline phase. Ceramic samples with the same amount of Er^{3+} as acceptor cation (S1 and S4) exhibit small-intensity peaks of the pyrochlore phase (highlighted in red). In general, the secondary phases observed in co-doped titanium dioxide have been understood as a consequence of the large size mismatch among the host cation (Ti^{4+}) and the dopants [27,28]. In this case, the ionic radii in 6-fold coordination are: 0.605 Å (Ti^{4+}), 0.64 Å (Ta^{5+}) and 1.03 Å (Er^{3+}) and, therefore, Er^{3+} substitution for Ti^{4+} in the [TiO_6] octahedron is expected to be too limited. As shown in Fig. 1, sample S3 with a lower content of Er^{3+} is a single-phase ceramic. Meanwhile, sample S2 amid Pr^{3+}/Pr^{4+} as acceptor cation, with relatively high ionic radii (1.13 Å and 0.99 Å for Pr^{3+} and Pr^{4+}, respectively), is also single-phase. Then, besides the size mismatch among the Ti^{4+} host and the dopants, other effects such as the solubility and valence of acceptor cations, energies for secondary phase formation and sintering temperature, may also contribute to the observed results. No other secondary phase was detected in the XRD patterns within the experimental limitations of the technique.

The phase composition was also investigated by XRD for sample S4 after a smooth sanding to remove a few micrometers from the external surface. Fig. 2(a) shows the diffraction pattern characteristics of the tetragonal structure of TiO_2, without the peaks (222) and (440) attributed to the pyrochlore $Er_2Ti_2O_7$ phase. Fig. 2(b) is a Raman spectrum of the same sample (S4), obtained after sanding the surface. The four active Raman modes in pure rutile TiO_2 are B_{1g} (~143 cm^{-1}), due to O–Ti–O bond bending; E_g (~447 cm^{-1}) due to oxygen atom liberation along the c-axis; A_{1g} (~612 cm^{-1}) related to Ti–O stretch mode, and the B_{2g} (~826 cm^{-1}) [29]. The Raman band at ~239 cm^{-1} is associated with a second order scattering in rutile, due to internal stress/strain and partial reduction of TiO_2 [30]. These results corroborate the tetragonal structure of rutile as major phase and reveal that the pyrochlore phase is preferentially formed on the surface of TiO_2 samples containing Er^{3+}.

Table 1 summarizes the identified crystalline phases in the XRD patterns of the as-prepared samples, the relative density (ρ_r) and the residual porosity (p_a) values of sintered ceramics.

In general, the relative density of all ceramics is high (> 94 % of the theoretical value) and the residual porosity is low (< 2 %). The lowest density and highest porosity were obtained for samples with excess Ti (S4), whereas the highest density and lowest porosity were found in ceramics with the highest content of the donor cation (S3). These results suggest that tantalum is beneficial for densification of co-doped TiO_2.

Fig. 3 shows SEM micrographs of polished and etched surfaces of sintered samples. The morphology of grains is predominantly polygonal with an average size in the 5–6 μm range for samples S1, S2 and S3.

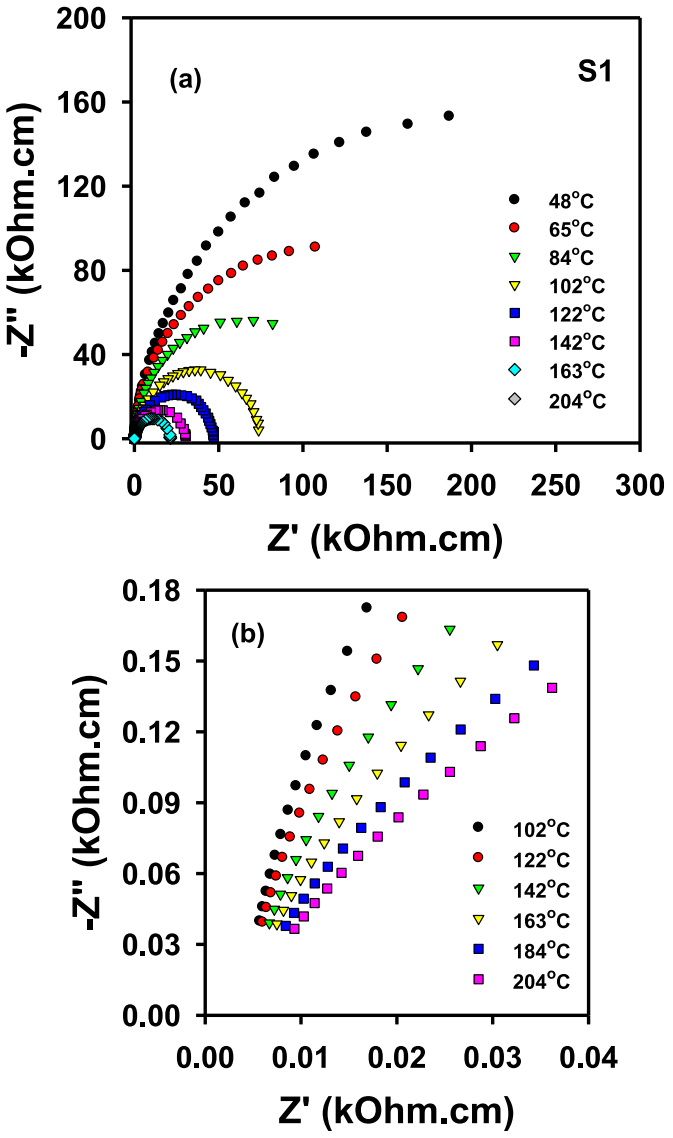

Fig. 4. (a) Impedance spectroscopy spectra of sample S1; (b) expanded view of the high-frequency impedance spectra above 100 °C.

Sample S4 shows a larger grain size compared to other samples and grain pullout. This effect may be attributed to excess Ti in this sample. Secondary phases are observed along the grain boundaries and triple grain junctions, evidencing the low solubility of the co-dopants in TiO_2. The secondary phase was not detected by XRD in sample S2 (Fig. 1) possibly owing to its low concentration and/or because it was not preferentially formed at the outer surface. Porosity is negligible for samples S1, S2 and S3, in agreement with results in Table 1. Sample S4 shows porosity inside the grains revealing a fast grain growth, due to accelerated migration of the grain boundaries during sintering. Fig. S1 (supplementary file) shows the EDS results for samples S1 (top) and S4 (bottom). In the left side are the microregions chosen for elemental mapping. Apparently, the dopants (Er and Ta) are randomly distributed with slight preference for grain boundaries.

In the complex plane, the -Z''(ω) x Z′(ω) plots of sample S1 measured at several temperatures are shown in Fig. 4. A single and large semicircular arc is observed in the frequency range of measurements, Fig. 4 (a), corresponding to the resistive and capacitive effects of the grain boundaries and interfaces (hereafter referred simply as interfaces). In addition, an expanded view of the high-frequency region (>100 kHz) of the impedance spectra measured above 100 °C is depicted in Fig. 4(b),

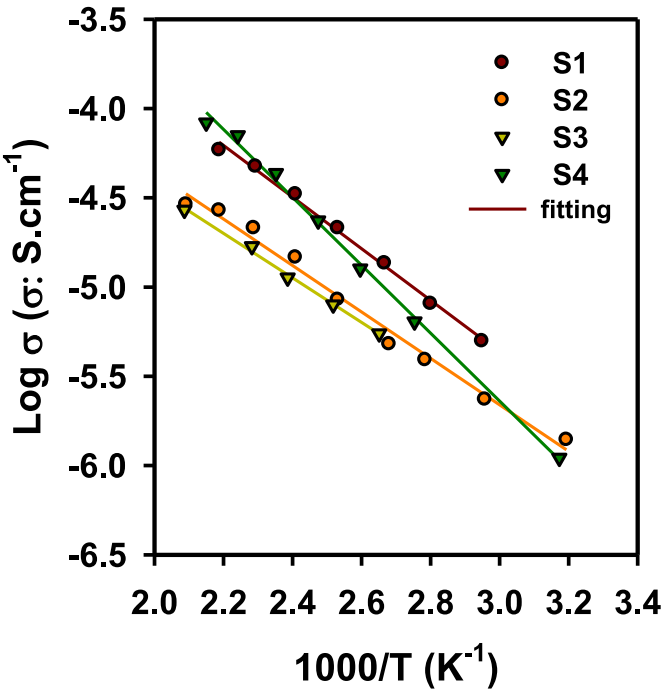

Fig. 5. Arrhenius plots of the electrical conductivity of sintered samples.

Table 2
Values of capacitance (C_i) and activation energy (E_i) of interfaces, and electric permittivity (ε′) and dissipation factor (tan δ) @1 kHz and 65 °C of sintered samples.

Sample	C_i (nF/cm)	E_i (±0.05 eV)	ε' (10^4)	tan δ
S1	9.40	0.29	11.7	0.153
S2	5.20	0.26	10.9	0.119
S3	7.40	0.25	6.85	0.152
S4	9.01	0.38	8.75	0.124

evidencing a non-zero intercept, due to the low resistivity of the bulk. It is noticeable that the shift of the high-frequency intercept with the measuring temperature is sluggish. Therefore, the analysis of the impedance spectra at several temperatures was restricted for the interface arc. To accomplish that, an equivalent electric circuit consisting of a resistance in parallel with a constant phase element representing the deviation from an ideal capacitor behavior was used. The large difference in the resistivity of the bulk and interfaces is mostly associated to heterogeneities such as amorphous or crystalline secondary phases, impurities, pores and others, which may contribute to the Maxwell-Wagner type effect. The impedance spectroscopy spectra in Fig. 4 are like those of other dielectric ceramics, where the IBLC model plays a role [31,32]. The interface resistivity decreases with increasing the temperature of measurements revealing a thermally activated process. Other samples studied (S2 to S4) show alike impedance spectroscopy behavior.

Fig. 5 shows the Arrhenius plots of the electrical conductivity of sintered samples in the 40 to ~215 °C range, obtained by fitting the impedance spectra. Single straight lines were found for all samples in the limited temperature range of measurements, and are approximately parallel to each other for samples S1, S2 and S3, emphasizing similar activation energy values. The interfaces of sample S4 seem to be more heterogeneous compared to other samples, leading to higher activation energy for conduction. This result may be attributed to a change in the concentrations of Ti^{3+} and oxygen vacancies compared to other samples due to excess Ti, and to a less extent, to the porosity of sample S4.

Table 2 summarizes the interface capacitance and activation energy values determined for all samples. The activation energies correlate to

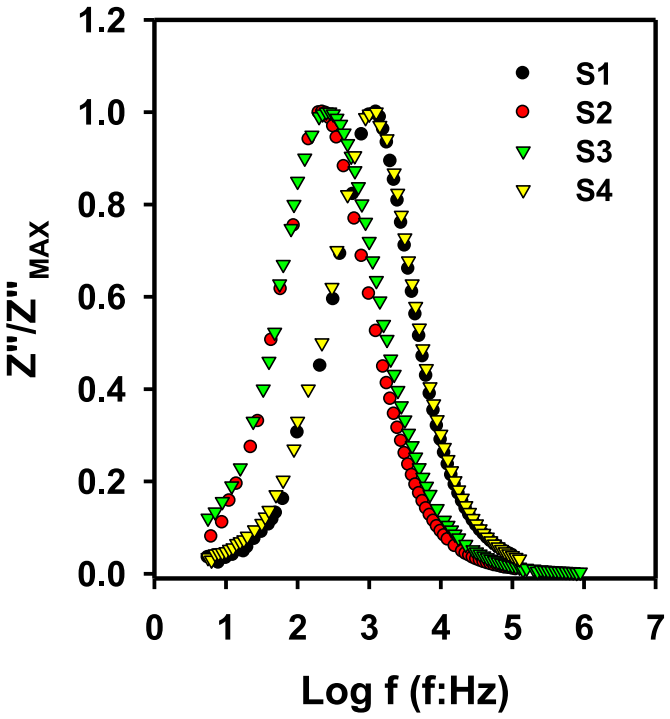

Fig. 6. Spectroscopic plot of the normalized complex impedance of sintered samples.

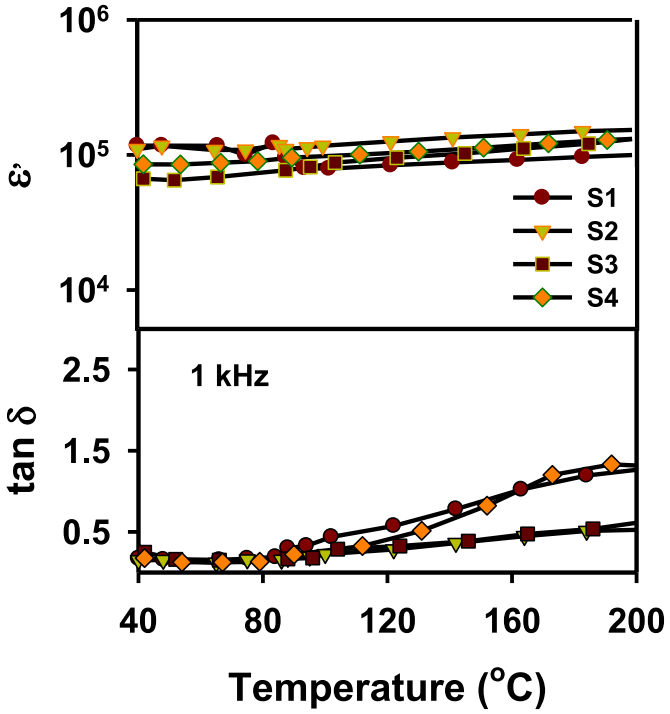

Fig. 7. Temperature-dependence of the electric permittivity (ε′) and dissipation factor (tan δ) of sintered samples at 1 kHz.

those of other co-doped TiO_2 ceramics [20,22–24]. The interface capacitances are in the nano Farad range, as expected [33].

Fig. 6 shows spectroscopic normalized complex impedance (Z''/Z''_{MAX}) plots at ~ 210 °C. All samples display a single Debye-like peak in the frequency range of measurements. The maximum amplitude of the normalized complex impedance peak for sample S1 is found slightly

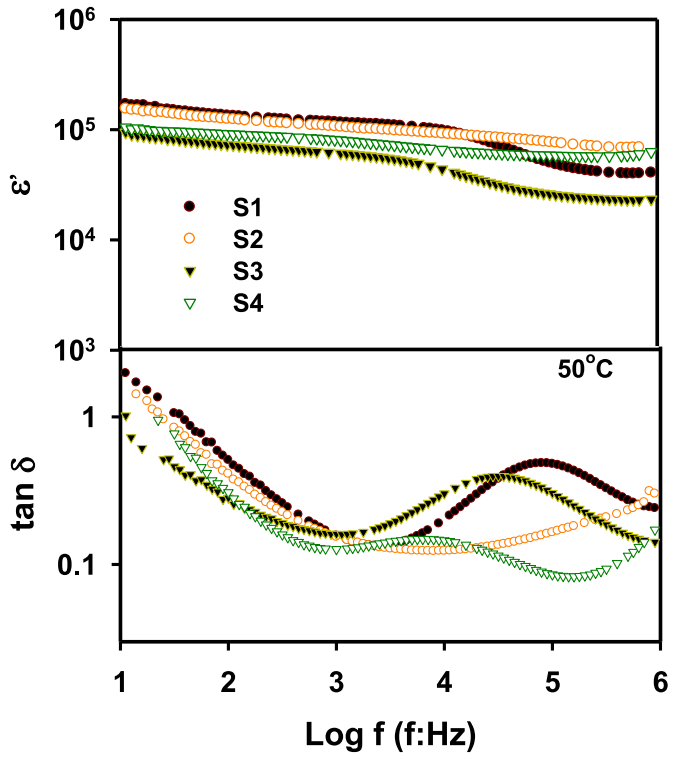

Fig. 8. Frequency-dependence of the electric permittivity (ε′) and dissipation factor (tan δ) of sintered samples at 50 °C.

above 1 kHz and matches that of sample S4. The same occurs for samples S2 and S3, but at a lower frequency. This variation in the frequency of the normalized complex impedance peaks seems to be related to the secondary phase ($Er_2Ti_2O_7$) detected by XRD (Fig. 1).

The temperature-dependence of the electric permittivity and dissipation factor of sintered samples at 1 kHz are depicted in Fig. 7. Irrespective of the composition, all the samples show colossal permittivity (Fig. 7, top) with an almost temperature-independent character in a wide range. The dissipation factor (Fig. 7, bottom) is rather constant up to approximately 100 °C and increases for higher temperatures. That increase is faster for samples S1 and S4, suggesting that the dissipation factor is dominated by the heterogeneous interfaces of those samples.

Table 2 summarizes values of the electric permittivity and dissipation factor at 1 kHz and 65 °C. Samples S1 and S3 with dissimilar amounts of the same co-dopants do not exhibit a significant difference in the dissipation factor, but over 40 % decrease of the electric permittivity by decreasing (about 50 %) the amount of the acceptor cation. Sample S4 with similar amounts of the same co-dopants as sample S1 but with excess Ti, shows decrease in both ε′ and tan δ. Besides that, the electric permittivity of sample S4 is still high, possibly due to its large grain size. Accumulation of charged defects (Ti^{3+}) near grain boundaries, due to excess Ti, may lead to the formation of space charge layers and the consequent decrease of the dissipation factor. It is worth noting that Er^{3+} (sample S1) is slightly more efficient than Pr (sample S2) to increase both ε′ and tan δ.

The frequency-dependence of the electric permittivity and the dissipation factor of co-doped TiO_2 recorded at ~50 °C are shown in Fig. 8. Samples S1 and S3 display slight decreases in the electric permittivity over 10 kHz, and a corresponding peak on the dissipation factor. Other co-doped TiO_2 ceramic systems show analogous behavior, which has been explained based on the several polarizations acting on the ceramic material [16,20–22,34]. At high frequencies, mostly higher than 10^5 Hz, ε′ is due to the bulk contribution, and interfacial polarization is no longer effective promoting a decrease in the electric permittivity. For samples S2 and S4, the electric permittivity is

approximately constant in the whole frequency range. This may be understood as a small influence of the interfacial polarization on these samples with excess Ti (S4) and with Pr (S2).

The overall results point to the influence of the type and concentration of dopants and sample composition on the electrical and dielectric properties of co-doped TiO_2, allowing for understanding and optimizing its performance as a dielectric ceramic. Moreover, the above results pointed that both mechanisms IBLC and EPDD act on (Er, Pr, Ta) co-doped TiO_2, and that the extent of each mechanism relies on several factors, such as dopants type and contents, and their distribution in the TiO_2 ceramic.

4. Conclusions

Dense ceramic samples consisting of titanium dioxide co-doped with erbium, praseodymium and tantalum oxides were successfully prepared by the solid-state synthesis method. A pyrochlore-type secondary phase was detected in samples containing 0.5 mol% Er^{3+}. Microstructure analysis evidenced the secondary phases at the grain boundaries and triple grain junctions. Impedance spectroscopy spectra revealed that the interfaces of the ceramic samples were substantially more resistive than the bulk. Activation energies for interfaces are 0.25–0.29 eV for samples S1, S2 and S3, and 0.38 eV for sample S4. All co-doped samples exhibited colossal permittivity ($>10^4$) and dissipation factor below 0.2. Samples with different contents of co-dopants show similar dissipation factor, but quite different electric permittivity. The temperature-dependence of the electric permittivity is approximately constant over wide ranges of temperature and frequency.

CRediT authorship contribution statement

Lucas A.S. Ferreira: Methodology, Investigation, Data curation. **Reginaldo Muccillo:** Writing – review & editing, Validation, Funding acquisition, Formal analysis. **Eliana N.S. Muccillo:** Writing – review & editing, Writing – original draft, Validation, Supervision, Investigation, Funding acquisition, Formal analysis, Data curation, Conceptualization.

Funding

Financial supports for this work were provided by FAPESP (proc. nº 2013/07692-2 and 2023/14931-8), CNPq (proc. nº 305557/2022-0, 306894/2023-8), FINEP (proc. nº 01.18.0073.00), CAPES (finance code 0001) and CNEN.

Declaration of competing interest

The authors declare that they have no known competing financial interest or personal relationships that could have appeared to influence the work reported in this paper.

Acknowledgements

The authors acknowledge the Center of Radiation Technology of IPEN for Raman spectroscopy measurements.

Appendix A. Supplementary data

Supplementary data to this article can be found online at https://doi.org/10.1016/j.jpcs.2025.113077.

Data availability

Data will be made available on request.

References

[1] S. Guillemet-Fritsch, Z. Valdez-Nava, C. Tenailleau, T. Lebey, B. Durand, J. Y. Chane-Ching, Colossal permittivity in ultrafine grain size $BaTiO_{3-x}$ and $Ba_{0.95}La_{0.05}TiO_{3-x}$ materials, Adv. Mater. 20 (2008) 551–555, https://doi.org/10.1002/adma200700245.

[2] S. Krohns, P. Lunkenheimer, S. Meissner, A. Reller, B. Gleich, A. Rathgeber, T. Gaugler, H.U. Buhl, D.C. Sinclair, A. Loidl, The route to resource-efficient novel materials, Nat. Mater. 10 (2011) 899–901, https://doi.org/10.1038/nmat3180.

[3] Y. Wang, W. Jie, C. Yang, X. Wei, J. Hao, Colossal permittivity materials as superior dielectrics for diverse applications, Adv. Funct. Mater. 29 (2019) 1808118, https://doi.org/10.1002/adfm.201808118.

[4] Z.J. Wang, M.H. Cao, Z.H. Yao, Q. Zhang, Z. Song, W. Hu, Q. Xu, H. Hao, H.X. Liu, Z.Y. Yu, Giant permittivity and dielectric loss of $SrTiO_3$ ceramics sintered in nitrogen atmosphere, J. Eur. Ceram. Soc. 34 (2014) 1755–1760, https://doi.org/10.1016/j.jeurceramsoc.2014.01.015.

[5] J. Wu, C.W. Nan, Y. Lin, Y. Deng, Giant dielectric permittivity observed in Li and Ti doped NiO, Phys. Rev. Lett. 89 (2002) 217601, https://doi.org/10.1103/PhysRevLett.89.217601.

[6] L. Zhang, Z.J. Tang, Polaron relaxation and variable-range-hopping conductivity in the giant-dielectric-constant material $CaCu_3Ti_4O_{12}$, Phys. Rev. B 70 (2004) 174306, https://doi.org/10.1103/PhysRevB.70.174306.

[7] M.F. Yan, W.W. Rhodes, Ultrahigh dielectric capacitance in TiO_2 ceramics, in: M. F. Yan, A.H. Heuer (Eds.), Additives and Interfaces in Electronic Ceramics, Adv. Ceram., vol. 7, The American Ceramic Society, Inc., Columbus, Ohio, USA, 1984, pp. 226–238. ISBN 0-916094-54-5.

[8] W. Hu, Y. Liu, R.L. Withers, T.J. Frankcombe, L. Norén, A. Snashall, M. Kitchin, P. Smith, B. Gong, H. Chen, J. Schiemer, F. Brink, J. Wong-Leung, Electron-pinned defect-dipoles for high-performance colossal permittivity materials, Nat. Mater. 12 (2013) 821–826, https://doi.org/10.1038/nmat3691.

[9] A.A. Zaki, H. Al-Refai, A.H. Bashal, M.A.H. Khalafalla, Tailoring optical and dielectric properties of TiO_2 through mono-and co-doping with Ag and Sr, J. Phys. Chem. Solid. 187 (2024) 111809, https://doi.org/10.1016/j.jpcs.2023.111809.

[10] P. Siriya, N. Chanlek, P. Thongbai, Giant dielectric properties and temperature stability of triple-doped $Al_xIn_{0.05-x}Ta_{0.05}Ti_{0.9}O_2$ ceramics, Ceram. Int. 50 (2024) 18977–18985, https://doi.org/10.1016/j.ceramint.2024.02.386.

[11] P. Xu, C. Guo, W. Hao, E. Cao, Enhancing grain boundary contributions to improve the dielectric properties of $(In_{0.5}Nb_{0.5})_{0.05}Ti_{0.95}O_2$ ceramics by Bi aided sintering, J. Phys. Chem. Solid. 187 (2024) 111881, https://doi.org/10.1016/j.jpcs.2024.111881.

[12] J. Fan, L. Zhong, T. Yang, Z. Hu, High breakdown electric field and ultralow loss in Sb+Ho co-doped TiO_2 giant dielectric ceramics induced by strongly coupled defect clusters, J. Materiomics 11 (2025) 100923, https://doi.org/10.1016/j.jmat.2024.07.008.

[13] D.C. Sinclair, T.B. Adams, F.D. Morrison, A.R. West, $CaCu_3Ti_4O_{12}$: One-step barrier layer capacitor, Appl. Phys. Lett. 80 (2002) 2153–2155. https://doi.org/10.1063/1.1463211.

[14] P. Lunkenheimer, V. Bobnar, A.V. Pronin, A.I. Ritus, A. Volkov, A. Loidl, Origin of apparent colossal dielectric constants, Phys. Rev. B 66 (2002) 052105, https://doi.org/10.1103/PhysRevB.66.052105.

[15] P. Lunkenheimer, S. Krohns, S. Riegg, S.G. Ebbinghaus, A. Reller, A. Loidl, Colossal dielectric constants in transition-metal oxides, Eur. Phys. J. Spec. Top. 180 (2010) 61–89, https://doi.org/10.1140/epjst/e2010-01212-5.

[16] W. Dong, W. Hu, A. Berlie, K. Lau, H. Chen, R.L. Withers, Y. Liu, Colossal dielectric behavior of Ga+Nb co-doped rutile TiO_2, ACS Appl. Mater. Interfaces 7 (2015) 25321–25325, https://doi.org/10.1021/acsami.5b07467.

[17] D.A. Crandles, S.M.M. Yee, M. Savinov, D. Nuzhnyy, J. Petzelt, S. Kamba, J. Prokes, Electrode effects in dielectric spectroscopy measurements on (Nb + In) co-doped TiO_2, J. Appl. Phys. 119 (2016) 154105, https://doi.org/10.1063/1.4947185.

[18] Z. Li, X. Luo, W. Wu, J. Wu, Niobium and divalent-modified titanium dioxide ceramics: colossal permittivity and composition design, J. Am. Ceram. Soc. 100 (2017) 3004–3012, https://doi.org/10.1111/jace.14850.

[19] L. Yuan, L. Li, G. Li, S. Wang, J. Li, D. Lu, W. Han, Optimizing giant dielectric properties via interface composition: A-study of rutile-based ceramics, Ceram. Int. 45 (2019) 17705–17714, https://doi.org/10.1016/j.ceramint.2019.05.338.

[20] W. Wang, L. Li, T. Lu, N. Zhang, W. Luo, Multifarious polarizations in high-performance colossal permittivity titanium dioxide ceramics, J. Alloys Compd. 806 (2019) 89–98, https://doi.org/10.1016/j.jallcom.2019.07.278.

[21] T. Nachaithong, P. Moontragoon, N. Chanlek, P. Thongbai, Fe^{3+}/Nb^{5+} Co-doped rutile-TiO_2 nanocrystalline powders prepared by a combustion process: preparation and characterization and their giant dielectric response, RSC Adv. 10 (2020) 24784, https://doi.org/10.1039/d0ra02963g.

[22] Y. Yu, Y. Zhao, Y.-L. Qiao, Y. Fen, W.-L. Li, W.-D. Fei, Defect engineering of rutile TiO_2 ceramics: route to high voltage stability of colossal permittivity, J. Mater. Sci. Technol. 84 (2021) 10–15, https://doi.org/10.1016/j.jmst.2020.12.046.

[23] K.N.D.K. Muhsen, R.A.M. Osman, M.S. Idris, Colossal permittivity and dielectric behaviour of $(Nb_{0.5}Fe_{0.5})_{0.1}Ti_{0.9}O_2$ and $(Ta_{0.5}Fe_{0.5})_{0.1}Ti_{0.9}O_2$ ceramics, J. Mater. Sci. Mater. Electron. 34 (2023) 777, https://doi.org/10.1007/s10854-023-10155-w.

[24] D.Y.B. Silva, R. Muccillo, E.N.S. Muccillo, Structural and dielectric properties of titania co-doped with yttrium and niobium: experimental evidence and DFT study, Ceramics 7 (2024) 411–425, https://doi.org/10.3390/ceramics7010026.

[25] F.M. Granozio, G. Koster, G. Rijnders, Functional oxide interfaces, MRS Bull. 38 (2013) 1017–1023, https://doi.org/10.1657/mrs.2013.282.

[26] R. Gerhardt, Impedance and dielectric spectroscopy revisited: distinguishing localized relaxation from long-range conductivity, J. Phys. Chem. Solid. 55 (1964) 1491–1506, https://doi.org/10.1016/0022-3697(94)90575-4.
[27] X. Cui, B. Guo, P. Liu, Y. Song, Low dielectric loss induced by annealing in $(La_{0.5}Nb_{0.5})_{0.005}Ti_{0.995}O_2$ colossal permittivity ceramics, J. Mater. Sci. Mater. Electron. 31 (2020) 2895–2903, https://doi.org/10.1007/s10854-019-02834-4.
[28] Z. Wan, H. Chen, W. Nian, J. Fan, Y. Li, X. Wang, X. Ma, Grain boundary effect on dielectric properties of $(Nd_{0.5}Nb_{0.5})_xTi_{1-x}O_2$ ceramics, J. Alloys Compd. 785 (2019) 875–882, https://doi.org/10.1016/j.jallcon.2019.01.243.
[29] A. Gajović, M. Stubićar, M. Ivanda, K. Furić, Raman spectroscopy of ball-milled TiO_2, J. Mol. Struct. 563/564 (2001) 316–320, https://doi.org/10.1016/S0022-2860(00)00790-0.
[30] Y. Zhang, C.H. Harris, P. Wallenmeyer, J. Murowchick, X. Chen, Asymmetrical lattice vibrational characteristics of rutile TiO_2 as revealed by laser power dependent Raman spectroscopy, J. Phys. Chem. C 117 (2013) 24015–24022, https://doi.org/10.1021/jp406948e.
[31] T.C. Porfirio, E.N.S. Muccillo, Effects of LiF addition on microstructure and dielectric properties of $CaCu_3Ti_4O_{12}$ ceramics, Ceram. Int. 42 (2016) 12005–12009, https://doi.org/10.1016/j.ceramint.2016.04.127.
[32] J. Fan, Z. Long, H. Zhou, G. He, Z. Hu, Colossal dielectric behavior of (Ho, Ta) co-doped rutile TiO_2 ceramics, J. Mater. Sci. Mater. Electron. 32 (2021) 14780–14790, https://doi.org/10.1007/s10854-021-06032-z.
[33] J.T.S. Irvine, D.C. Sinclair, A.R. West, Electroceramics: characterization by impedance spectroscopy, Adv. Mater. 2 (1990) 132–138, https://doi.org/10.1002/adma.19900020304.
[34] Z. Jiang, M. Shi, Z. Wan, J. Liu, L. Zhang, Y. Jiu, B. Tang, D. Xu, Giant dielectric permittivity of Ca and sb-co-doped TiO_2 ceramics, J. Mater. Sci. Mater. Electron. 33 (2022) 18389–18399, https://doi.org/10.1007/s10854-022-08693-w.